Article

Experimental Investigation on Corrosion Behavior of X80 Pipeline Steel under Carbon Dioxide Aqueous Conditions

Jukai Chen, Xiaodan Wang, Honglian Ma, Zhiyuan Huo, and Yueshe Wang*

Cite This: ACS Omega 2022, 7, 6142−6150

Read Online
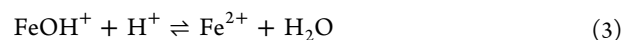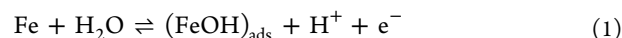
ACCESS | Metrics & More | Article Recommendations

ABSTRACT: A combined steady-state and transient approach is employed to investigate the corrosion behavior of X80 pipeline steel in carbon dioxide-saturated brines. Continuous bubbling of carbon dioxide into a test vessel with 1 liter capacity is performed to simulate the flowing condition. The measurement of time-dependent open-circuit potential, polarization resistance, and electrochemical impedance spectroscopy (EIS) is conducted to interpret the evolution of dissolution processes at the corroding interface. Three distinguishing stages are observed at a temperature of 60 °C during a whole exposure of 144 h. Analyses mainly based on the consecutive mechanism show that after the first stage of the active-adsorption state, the anodic reaction is significantly retarded by the accumulation of $(FeOH)_{ads}$ on the iron surface, causing a sharp increase in the polarization resistance and the open-circuit potential, as well as the disappearance of the inductive loop in EIS. At the third stage, the formation of the corrosion product layer similarly reduces both the anodic and cathodic reactions, which arouses a linear increase in the polarization resistance with time and a capacitive loop in EIS but changes the open-circuit potential slightly. An increase in salinity in this study reduces the polarization resistance and enhances iron dissolution by promoting the formation and relaxation of $(FeOH)_{ads}$; however, it brings little change to the developing time of the three stages obviously. At a low temperature of 20 °C, a protective product layer is not observed in carbon dioxide-saturated brine, and the dissolution of iron is mainly under activation control during the whole exposure. A notable enlarged polarization resistance and different interfacial processes are observed in an alkaline solution compared with those in acidic environments, which is deduced to be resulted from an impedance in the relaxation of $(FeOH)_{ads}$ by increasing pH. The observations in this study support well that the iron dissolution reaction at the initial stage exposed in carbon dioxide aqueous environments is dominant by water adsorption on the iron surface, and further investigation should be performed on the role that carbon dioxide plays in the evolution of corrosion products and the formation of a protective film on the steel surface by taking into account local water chemistry.
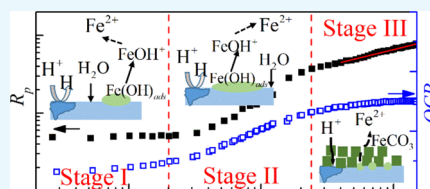
1. INTRODUCTION

An earlier investigation revealed that 28% of corrosion-related failures in the oil and gas industry are associated with carbon dioxide, which could be named "sweet corrosion."[1] In view of this, the problem of carbon dioxide corrosion has long been recognized and discussed since the last century. However, because of the complicated processes underlying carbon dioxide corrosion,[2] its mechanistic understanding is still in development.[3−7] In aqueous environments, the dissolved carbon dioxide is partially hydrated into carbonic acid, and carbonic acid is partially ionized to release protons as a weak acid, which is called water chemistry in carbon dioxide corrosion. The dissolved carbon dioxide and partially hydrated carbonic acid play a vital role in hydrogen evolution reaction, which is generally known as the "buffer" effect of carbon dioxide solution. Consequently, it is reported that under the same pH condition, corrosion in carbon dioxide-containing solutions is much more serious than that in strong acid solutions.[5,8] However, the role that carbon dioxide plays in the corrosion process is not totally understood till now. An opinion is that in acidic environments, carbon dioxide corrosion is dominated by hydrogen reduction, which is a

common acid corrosion mechanism. For instance, the "consecutive" mechanism proposed by Bockris[9] is widely adopted to analyze interfacial processes during carbon dioxide corrosion of carbon steels, as described in eq 1−3:

$$Fe + H_2O \rightleftharpoons (FeOH)_{ads} + H^+ + e^- \tag{1}$$

$$(FeOH)_{ads} \rightarrow FeOH^+ + e^- \tag{2}$$

$$FeOH^+ + H^+ \rightleftharpoons Fe^{2+} + H_2O \tag{3}$$

Eq 1 indicates that the dissolution of iron is stirred up by the adsorption of water on its free surface. Eq 2 is regarded as the subsequent relaxation of the adsorbed $(FeOH)_{ads}$, which will promote the adsorption action of water, as shown in eq 1, and
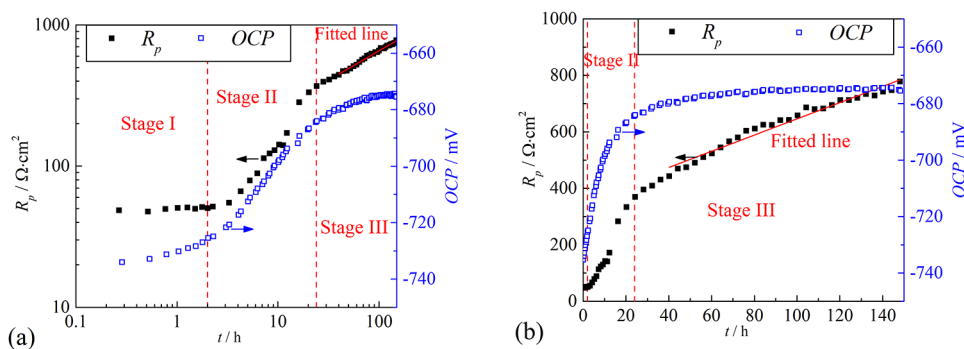
Figure 1. Evolution of polarization resistance (R_p) and OCP vs Ag/AgCl electrode of X80 steel exposed to a carbon dioxide-saturated 0.6 mol L^{-1} sodium chloride solution (T = 60 °C, P_{CO2} = 0.8 bar) both (a) in logarithmic and (b) in linear time scale.

increase the free surface area of iron. Obviously, the enhancement of the relaxation of $(FeOH)_{ads}$ can reduce charge-transfer resistance and bring in an inductive characteristic in electrochemical impedance measurement. Therefore, the observations of the inductive component in impedance behavior underlying anodic the dissolution of pure iron or steel in acidic solutions lend credence to the consecutive mechanism.[10−17]

In addition to the discussion of the underlying mechanism, the influence of such environmental factors as salinity and temperature on carbon dioxide corrosion has also attracted considerable attention. For instance, Liu et al. investigated the effects of the chloride content on carbon dioxide corrosion and showed that chloride has no effect on the composition of the corrosion product, which was always iron carbonate.[18] The protectiveness of iron carbonate is observed to be positively associated with temperature and pH, but the kinetics of its formation is pretty complex.[19] The existence of critical temperature for the formation of protective iron carbonate film has been widely observed, but divergent values are presented.[20−23] A flow cell integrated with in situ synchrotron radiation-X-ray diffraction (SR-XRD) and electrochemistry was employed by Burkle et al.[24] to study the precipitation kinetics of iron carbonate on the X65 carbon steel surface exposed in carbon dioxide-saturated brine at different pH and at 80 °C. The nucleation of iron carbonate was detected unexpectedly during the exposure, before the general corrosion rate evaluated by electrochemistry was evidently reduced. Moreover, the induction time of iron carbonate formation significantly decreased with increased pH. By taking the microstructure of steels into account, iron carbide is another key factor that affects the formation of the iron carbonate film. Experimental results indicated that iron carbonate was more easily precipitated on a surface with exposed iron carbide,[25] and a porous iron carbide layer created favorable conditions for the formation of protective iron carbide.[17,26]

However, despite the abovementioned studies, scarce information is available on the long-term evolution of the carbon dioxide corrosion of steels by in situ electrochemical tests. As suggested in the discussion on revealing iron dissolution mechanisms underlying carbon dioxide corrosion,[27,28] multiple information would be necessary to incorporate, especially through transient techniques, which is still insufficient.

In this study, both the steady-state linear polarization resistance (LPR) and the transient technique electrochemical impedance spectroscopy (EIS) measurement were employed

to investigate carbon dioxide-involved corrosion behavior of X80 steel, an increasingly used pipeline steel by petroleum industries in China, especially in the West-to-East natural gas transmission pipeline project. A continuous bubbling of carbon dioxide into the test vessel was implemented to simulate the flowing condition. The evolution of dissolution processes at the interface of the steel exposed in several carbon dioxide-saturated solutions with different salinity, temperature, and pH was analyzed by the impedance results.

2. EXPERIMENTAL SECTION

2.1. Material and Experimental Conditions. A three-electrode cell setup was adopted, of which the working electrode was made of an X80 steel specimen sealed in epoxy resin with an exposed area of 1 × 1 cm^2. A silver/silver chloride (saturated potassium chloride solution) electrode was used as the reference electrode, and a platinum electrode with an area of 1 × 1 cm^2 served as the counter electrode. The capacity of the test vessel is 1 L. Before each testing, the working electrode was ground successively with 400, 600, 800, 1000, 1200, and 1500 grit silicon carbide paper, rinsed with distilled water and alcohol, and dried with cold air. The electrolyte solution was made of sodium chloride dissolved in ultrapure water (produced by Direct-Q 3 UV, Millipore) with a concentration of 0.1 or 0.6 mol L^{-1} at a temperature of 60 or 20 °C. Both the working electrode and the electrolyte solution were prepared just before testing to make them fresh. Also, the electrolyte solution was bubbled with carbon dioxide for at least 3 h to deoxygenate. The bubbling was then kept at a flow rate of 20 mL min^{-1} till the end of the test.

2.2. Electrochemical Measurements. All the electrochemical experiments were conducted using a potentiostat (VersaSTAT3F, Princeton). The corrosion process was monitored by measuring the LPR and EIS. The polarization resistance R_p was measured by polarizing the working electrode from −15 to +15 mV vs open-circuit potential (OCP) at a scanning rate of 0.25 mV s^{-1}, also corrected by the solution resistance obtained from the EIS measurement. The corrosion rate (CR) could be evaluated approximately via the Stern−Geary equation by employing the measured R_p and a coefficient in the case of kinetic control. However, in this study, during 144 h exposure, the characteristic of the corrosion surface would have significantly changed along with the Stern−Geary coefficient. Thus, we just evaluated the maximum CR at the initial stage of exposure by adopting the Stern−Geary coefficient as 26 mV,[29] during which the steel surface was smooth and clean, and the corrosion would be

kinetically controlled. For EIS measurement, the frequency range started at 20 kHz and finished at 10 mHz. The amplitude of the applied sinusoidal voltage was 10 mV at the OCP.

3. RESULTS AND DISCUSSION

3.1. Polarization Resistance and the OCP. Three stages are observed from the evolution of polarization resistance (R_p) with time for X80 steel exposed to a carbon dioxide-saturated 0.6 mol L^{-1} sodium chloride solution at 60 °C, as shown in Figure 1. During the first 2 h, R_p changes slightly and stays at a low level, which indicates a high CR. As mentioned in Section 2.2, a maximum CR of 6.40 ± 0.25 mm y^{-1} can be obtained using the Stern−Geary equation with a coefficient of 26 mV. After that, R_p increases sharply until 24 h of exposure. Finally, the growth of R_p slows down again, and a linear increase appears within 40−144 h exposure. In the first two stages, the changes of OCP show a synchronous trend with R_p. The difference is that, in the third stage, the increase in the OCP slows down continuously, and the OCP almost becomes steady at the end of exposure with a total increase of 60 mV approximately.

3.2. Electrochemical Impedance Spectroscopy. In accordance with the evolution of R_p and the OCP at different exposure times of X80 steel in a carbon dioxide-saturated 0.6 mol L^{-1} sodium chloride solution (T = 60 °C, P_{CO2} = 0.8 bar), the evolution of EIS can also be divided into three distinguishable stages, as shown in Figure 2. In the first stage
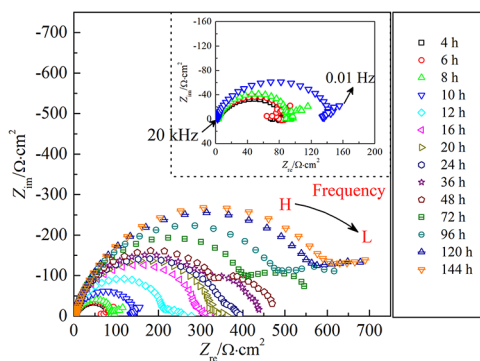

Figure 2. EIS results of X80 steel in a carbon dioxide-saturated 0.6 mol L^{-1} sodium chloride solution (T = 60 °C, P_{CO2} = 0.8 bar).

(i.e., the first 10 h of exposure), the Nyquist plot is characterized by a depressed semicircle at high frequencies, an inductive loop at low frequencies, and another capacitive loop at even lower frequencies. In the second stage (i.e., 12−24 h of exposure), the inductive loop and the capacitive loop in the lower frequency range both disappear, and only one capacitive semicircle can be distinguished. Remarkably, the Nyquist plots at 12−20 h of exposure show a "tail" that drifts near the x-axis at low frequencies, which is caused not by the system error but by the change in the polarization resistance during the measurement. After 12 h of exposure, the number of cycles for which the data are collected and averaged is adjusted from 1 to 6. This adjustment aims at improving the data quality, especially in the low-frequency range. Correspondingly, the measuring time of EIS for one case is increased from 30 min to 3 h approximately, and most of the time costs at the low-frequency measurement. At the same time, the polarization resistance increases remarkably, as shown in Figure 1, which indicates a significant increase in the impedance at low

frequencies during the measurement.[30] It reflects such a "tail" on the Nyquist plot. In the third stage (after 24 h of exposure), the Nyquist diagram is characterized by two capacitive loops, one in the high-frequency range and one in the low-frequency range.

3.3. Equivalent Circuit for Modeling the EIS Results. For the first stage of EIS changes during exposure, the capacitive semicircle in the high-frequency range characterizes the capacitance effect of the double layer; the inductive loop in the low-frequency range is usually believed to be associated with the relaxation of the intermediate $(FeOH)_{ads}$ during iron dissolution;[5,11] and another capacitive loop in the lower frequency range is related to the adsorption of other corrosion intermediates or the formation of the corrosion product.[5,12,16,31,32] However, this corrosion intermediate or product is not so much stable because after 10 h of exposure, the inductive loop and the capacitive loop in the low-frequency range both disappear. It is also possible that the capacitive loop in the low-frequency range is dependent on the inductive loop, which means that the capacitive loop in the low-frequency range seems to be associated with the transformation of the adsorbed species $(FeOH)_{ads}$.[11] An equivalent circuit is presented in Figure 3 for modeling the EIS results at the
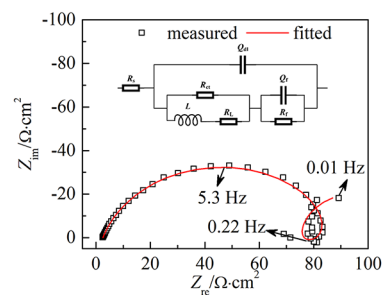

Figure 3. Equivalent circuit for the first-stage modeling and the example of EIS data fitting (at 4 h of exposure).

first stage, the element R_s of which represents the solution resistance, Q_{dl} represents the double-layer capacitance, R_{ct} represents the charge-transfer resistance, R_L represents the inductive resistance, and R_f represents the resistance of the adsorbed intermediate product.

The equivalent circuit for modeling the EIS results in the second stage is quite simple, as presented in Figure 4. The appearance of "tail" drifting near the x-axis at low frequencies is discussed in Section 3.2. During this stage, there is no stable protective corrosion product formed on the specimen surface.
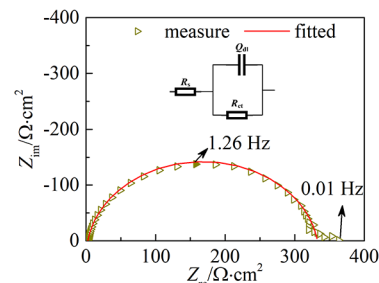

Figure 4. Equivalent circuit for the second-stage modeling and the example of EIS data fitting (at 20 h of exposure).

After 24 h of exposure, another capacitive loop arises at low frequencies, which demonstrates the formation of a porous product layer on the electrode surface. The equivalent circuit for the third-stage modeling is presented in Figure 5, where R_f represents the resistance of the corrosion product layer. Under this condition, the polarization resistance R_p can be calculated using the following equation:
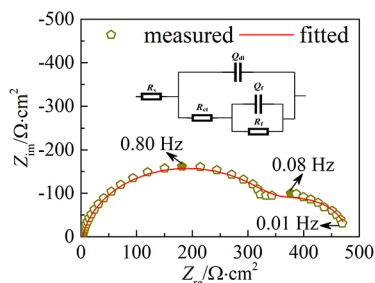
$$R_p = R_{ct} + R_f \tag{4}$$

Figure 5. Equivalent circuit for the third-stage modeling and the example of EIS data fitting (at 48 h of exposure).

From eq 4, it can be perceived that R_p is highly dependent on R_f, which means the larger R_f, the larger R_p, the more protective the corrosion scale. The value of R_f can be approximately estimated by the diameter of the second capacitive semicircle. As can be seen from Figure 2, R_{ct} and R_f increase gradually with exposure time, corresponding to the increase in R_p, as shown in Figure 1.

3.4. Effects of Salinity, Temperature, and pH.
3.4.1. Effect of Salinity.
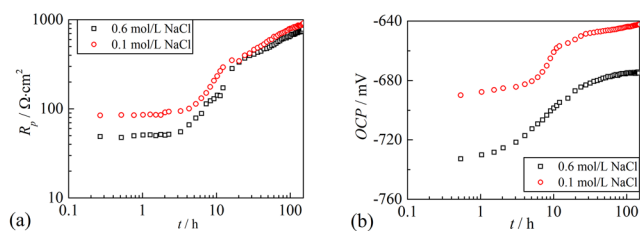It can be observed from Figures 6

Figure 6. Comparison of (a) the polarization resistance R_p and (b) the OCP of X80 steel exposed in the carbon dioxide-saturated brines with different salinities (i.e., 0.6 or 0.1 mol L^{-1} sodium chloride; T = 60 °C, P_{CO2} = 0.8 bar).

and 7 that the corrosion behavior of X80 steel exposed in the carbon dioxide-saturated brines with different salinities is quite similar. The minor differences are that the maximum CR at the initial exposure in the 0.1 mol L^{-1} sodium chloride solution is 3.59 mm y^{-1}, nearly 44% decrease compared with that in the 0.6 mol L^{-1} sodium chloride solution (6.40 mm y^{-1}); the OCP in the 0.1 mol L^{-1} sodium chloride solution is always more positive than that in the 0.6 mol L^{-1} sodium chloride solution; the capacitive loop in the low-frequency range caused by the formation of the corrosion scale appears more lingeringly in the 0.1 mol L^{-1} sodium chloride solution (compare the Nyquist plot at 48 h of exposure with that in the 0.6 mol L^{-1} sodium chloride solution, in Figure 7), which may mainly be attributed to the lower CR and the less release of the ferrous ion. A nobler OCP to some extent could account for better thermodynamic stability in corrosion. It means that the
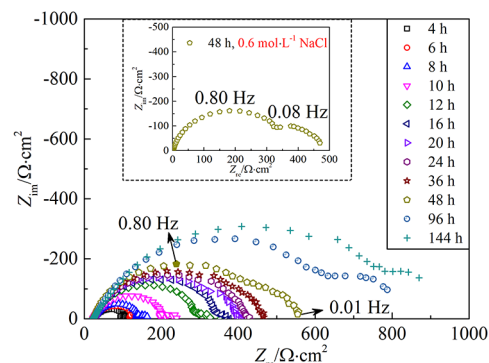

Figure 7. EIS results of X80 steel in a carbon dioxide-saturated 0.1 mol L^{-1} sodium chloride solution (T = 60 °C, P_{CO2} = 0.8 bar).

increase in the chloride ion concentration from 0.1 to 0.6 mol L^{-1} can promote the corrosivity of the carbon dioxide aqueous environment. However, a further increase in the chloride ion concentration will reduce carbon dioxide solubility and hamper the CR from increasing continually,[18] which is beyond the scope of this work.

For a more detailed comparison, the fitted data of EIS results at the first stage are listed in Table 1. The charge-transfer resistance R_{ct} in 0.6 mol L^{-1} sodium chloride solution is lower than that in 0.1 mol L^{-1}, in accordance with a higher CR at the initial stage of the former than the latter. The inductance value in 0.6 mol L^{-1} sodium chloride solution is nearly four times that in 0.1 mol L^{-1} solution. As mentioned before, the inductive behavior is regarded to be attributed to the relaxation of water−iron species $(FeOH)_{ads}$. A greater inductance indicates an enhanced relaxation of $(FeOH)_{ads}$, which signifies an increase in active sites on the corroding surface in 0.6 mol L^{-1} sodium chloride solution. An increase in the capacitance Q_f and resistance R_f related to the adsorbed intermediate product is also observed in 0.6 mol L^{-1} sodium chloride solution, which may be resulted from a more rapid accumulation of the product in this case.

In Figure 8, the characteristic frequencies are marked on the Nyquist plot for the comparison of the time constants at the first stage between the two salinities. The time constants become greater when the salinity increases from 0.1 to 0.6 mol L^{-1}, particularly in the low-frequency range. There are three constants in the anodic process at 0.1 mol L^{-1}, while only two are observed at 0.6 mol L^{-1}. It is probably because the measurements are conducted at the lowest frequency of 0.01 Hz, which is obviously higher than the hidden time constant at lower frequencies at 0.6 mol L^{-1}. The difference between the two cases reflected by inductive and capacitive characteristics in the low-frequency range shows that the salinity, or rather the concentration of chloride ions, has a subtle impact on the formation and relaxation of the intermediate product $(FeOH)_{ads}$ during carbon dioxide corrosion.

3.4.2. Effect of Temperature.
The EIS results of X80 steel exposed in carbon dioxide-saturated sodium chloride solution at a temperature of 20 °C are illustrated in Figure 9. In comparison with that shown in Figure 7 at 60 °C, the Nyquist plot with two capacitive loops is hardly observed within the whole exposure duration of 144 h. The diameter of the semicircle shown in Figure 9, which represents the charge-transfer resistance, increases gradually with exposure time, similar to the observations at a temperature of 60 °C, but much larger at a temperature of 20 °C. It is reported that the

Table 1. Comparison of the Fitting Data at the First Stage between Different Salinities

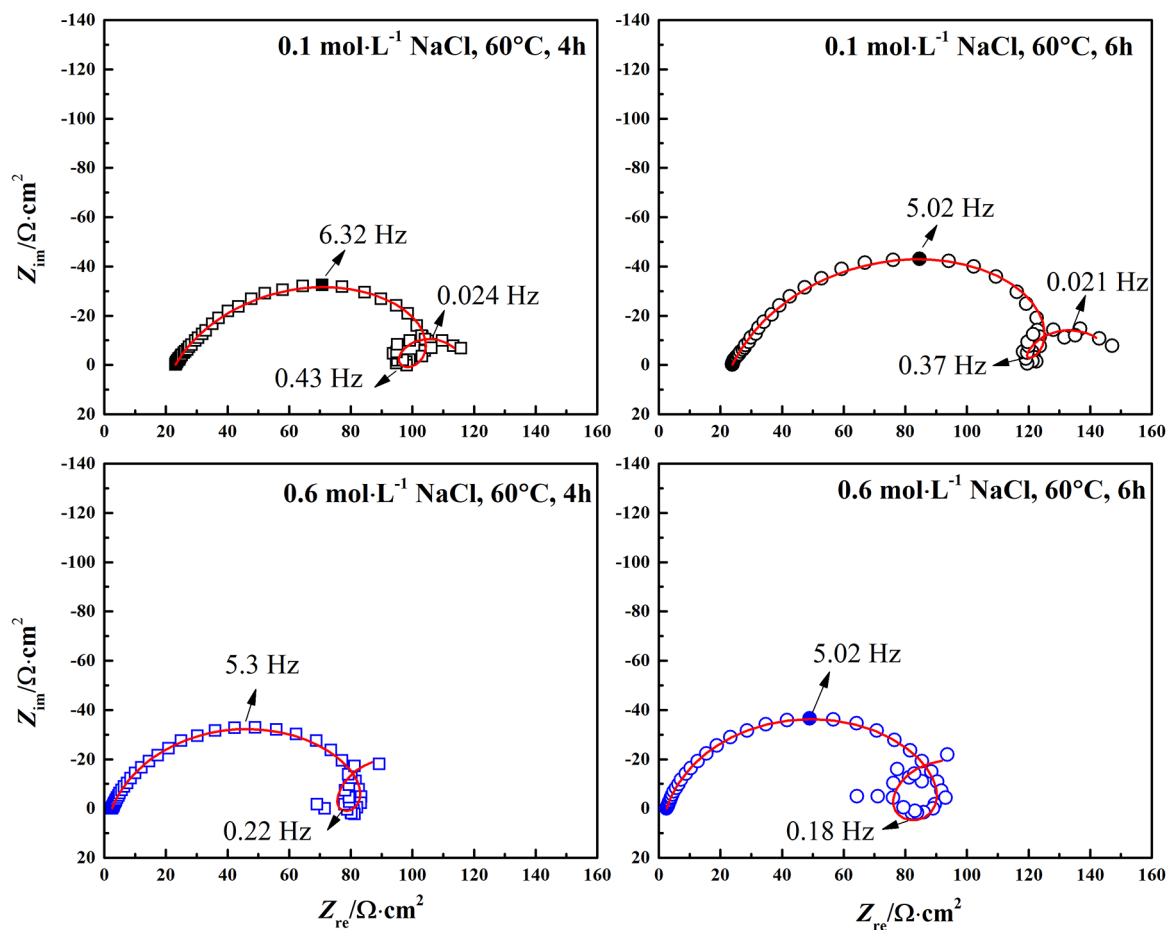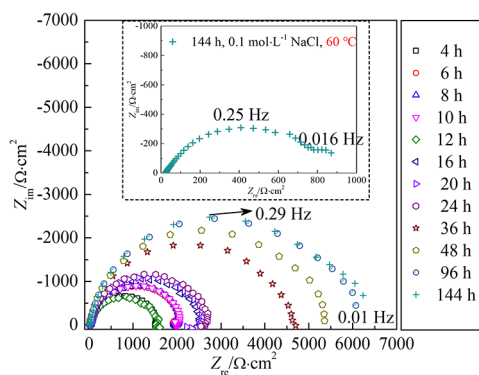| C_{NaCl}	t	Q_{dl}	n_1	R_{ct}	Q_f	n_2	R_f	L	R_L
(mol L^{-1})	(h)	(μF cm^{-2} s^{n1-1})		(Ω cm^2)	(μF cm^{-2} s^{n2-1})		(Ω cm^2)	(H cm^2)	(Ω cm^2)
0.1	4	798.4	0.72	101.8	2.81×10^5	1	20.35	65.10	256.6
	6	649.6	0.76	129.7	2.89×10^5	1	26.66	75.55	385.0
0.6	4	655.1	0.81	88.19	5.72×10^5	0.98	41.79	239.4	414.8
	6	596.6	0.84	94.18	4.23×10^5	0.99	40.96	277.1	296.1

Figure 8. Comparison of EIS results at the first stage between different salinities.

Figure 9. EIS results of X80 steel in a carbon dioxide-saturated 0.1 mol L^{-1} sodium chloride solution (T = 20 °C, P_{CO2} = 0.98 bar).

solubility limit of iron carbonate is negatively correlated with temperature,[33] and at a temperature below 40 °C, a protective film is hard to form.[19,20] The EIS results in this study show that the decrease in the CR at low temperatures is not attributed to the formation of the corrosion scale or its blocking for the corrosive species to the metal surface. In this case, the value of polarization residence R_p is approximately equal to the charge-transfer resistance R_{ct}. Meanwhile, the corrosion process is mainly activation-controlled.

3.4.3. Effect of pH. In this study, sodium bicarbonate is added to adjust the pH of the testing solution to be alkaline. A mixed solution with concentrations of 0.6 mol L^{-1} sodium chloride and 1 mol L^{-1} sodium bicarbonate is used to study the corrosion behavior of X80 in the carbon dioxide-containing alkaline environment. The pH of this testing solution is 7.6, which is determined by the water chemistry calculation underlying carbon dioxide corrosion, which performs well in our previous work.[34] The EIS measurement under this condition is demonstrated in Figure 10. In alkaline solution, the first step of iron dissolution could be assumed as given in eq 5.
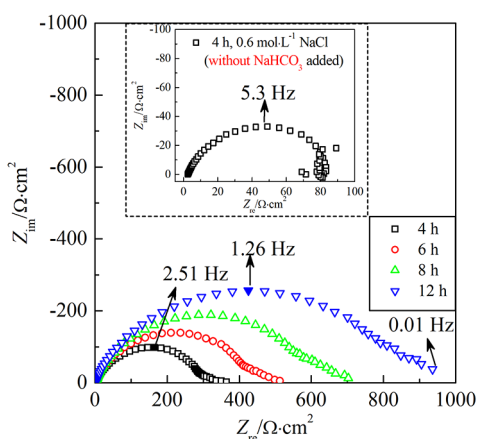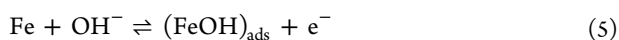
$$Fe + OH^- \rightleftharpoons (FeOH)_{ads} + e^- \qquad (5)$$

Figure 10. EIS results of X80 steel in a carbon dioxide-saturated 0.6 mol L^{-1} sodium chloride and 1 mol L^{-1} sodium bicarbonate mixed solution (T = 60 °C, P_{CO2} = 0.8 bar).

Under alkaline conditions, the adsorbed species $(FeOH)_{ads}$ would be rapidly formed, cover the surface, and accumulate shortly after exposure, while the relaxation of $(FeOH)_{ads}$ does not significantly change the coverage of $(FeOH)_{ads}$. As a result, the inductive loop is not distinguishable enough. The Nyquist plot is characterized by one highly depressed semicircle. The polarization resistance, as the Z_{re}-intercept of the Nyquist plot, increases rapidly and brings an evident "tail," followed by the depressed semicircle. From the Nyquist plot shown in Figure 10, it is also observed that the diameter of the semicircle is several times larger than that in the acid solution at the same temperature (Figure 2), while the OCP in alkaline solution is several tens of mV negative than that in acid solution (as shown in Figure 11). The characteristic frequency of the
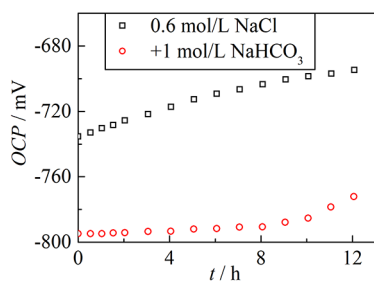

Figure 11. OCP of X80 steel in a carbon dioxide-saturated 0.6 mol L^{-1} sodium chloride and 1 mol L^{-1} sodium bicarbonate mixed solution (T = 60 °C, P_{CO2} = 0.8 bar).

capacitive loop at the initial exposure stage in alkaline brine is much lower than that in acid (Figure 10), which indicates a significant change in interfacial processes aroused by increasing pH.

3.5. Discussion. As can be seen from Sections 3.1 and 3.4.1, the polarization resistance R_p and the OCP increase dramatically after several hours of exposure in both 0.6 and 0.1 mol L^{-1} sodium chloride carbon dioxide-saturated solutions (T = 60 °C, P_{CO2} = 0.8 bar). However, after dozens of hours, R_p increases linearly with further exposure, while the OCP tends to be steady. Here, we employ an Evans diagram to interpret the origin of the evolution difference between R_p and the OCP.

In view of the "buffer" effect induced by dissolved carbon dioxide and the excellent diffusion capability of hydrion, we do not consider the case of concentration polarization in this study. As shown in Figure 12, either the anodic or the cathodic polarization curve moving left brings a decrease in the corrosion current density, in other words, an increase in R_p. The point is that, as shown in Figure 12a, the anodic reaction is reduced more than the cathodic reaction as the anodic curve moves more to the left, which increases the corrosion potential ($E_{corr2} > E_{corr1}$). By contrast, as shown in Figure 12b, the cathodic reaction is reduced more than the anodic reaction as the cathodic curve moves more to the left, lowering the corrosion potential ($E_{corr2} < E_{corr1}$).

Therefore, from Stage I to Stage II (as illustrated in Figure 1), the anodic reaction is retarded more significantly than the cathodic reaction, and it arouses a great increase in the corrosion potential, as shown in Figure 13. From Stage II to Stage III, both the anodic and cathodic reactions are reduced similarly, and the corrosion potential changes slightly.

Combining with the results of EIS, the interfacial processes underlying this behavior are described as given below. In the first stage, the steel surface is at an active-adsorption state. According to the consecutive mechanism, water adsorbs on the free iron surface, which facilitates an intermediate $(FeOH)_{ads}$ as the first step of iron dissolution in the acid solutions. Obviously, the increasing coverage of $(FeOH)_{ads}$ on the free iron surface hinders the first dissolution step, mainly affecting the anodic reaction area (developing from Stage I to Stage II, Figure 14). As a Faradaic process, it will increase the charge-transfer resistance R_{ct} and enlarge the diameter of the capacitive loop in the Nyquist plot. However, in another Faradaic process, as described in eq 2, the relaxation of $(FeOH)_{ads}$ reduces the coverage on the free iron surface, promotes the dissolution, as well as reduces the polarization resistance R_p, which reflects on an inductive loop in the Nyquist plot.

As $(FeOH)_{ads}$ gradually accumulates on the free iron surface and is overproduced, the relaxation of accumulated $(FeOH)_{ads}$ brings an insignificant effect on the coverage, and the inductive loop disappears. In this stage, the accumulation of $(FeOH)_{ads}$ on the iron surface inhibits the reaction of water adsorption, and the anodic process becomes the control step of corrosion, which is similar to the case sketched in Figure 12a.

When the released ferrous ion is enough to exceed the solubility of iron carbonate, precipitation takes place (Stage II → III, Figure 14). Together with the insoluble microstructures (such as cementite), the precipitated corrosion products compose a porous layer covering the metal surface. Unlike the intermediate $(FeOH)_{ads}$ only adsorbed on the free iron surface, this porous layer covers both the anodic and cathodic areas, and the blocking effect reduces the anodic and cathodic reactions similarly. As a result, the corrosion potential changes slightly in this period (developing from Stage II to Stage III, Figure 13). The porous layer is characterized by a newly arising capacitive loop in the Nyquist plot, as shown in Figure 5, the resistance R_f of which is associated with the coverage, thickness, and microstructure of this porous layer.

In comparison with that in 0.1 mol L^{-1} sodium chloride solution, the increase in salinity to 0.6 mol L^{-1} promotes the relaxation of $(FeOH)_{ads}$, as mentioned in Section 3.4.1; however, the synchronous evolution of R_p and the OCP of the two cases, as shown in Figure 6, indicate that the increase in salinity must promote the formation of $(FeOH)_{ads}$ similarly
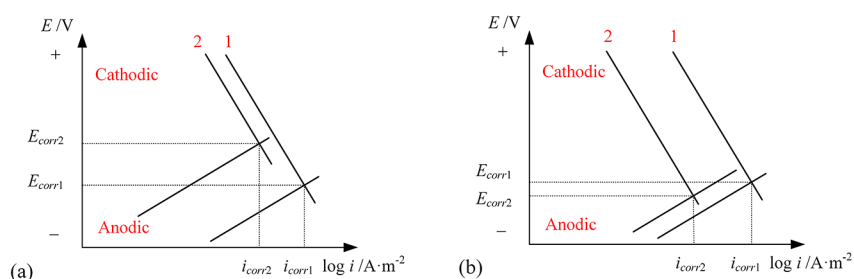
Figure 12. Evans diagrams for interpreting two different scenarios in which an increase in R_p is accompanied by (a) an increase or (b) a decrease in the corrosion potential.
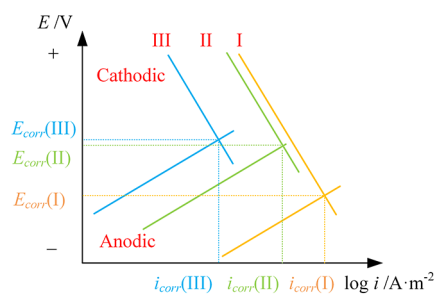

Figure 13. Evolution of polarization curves from Stage I to Stage III of X80 steel exposed in carbon dioxide-saturated brines.

[the first step of the consecutive mechanism, as written in eq 1].

At a low temperature of 20 °C, a protective product layer is never observed in this study, that is, the high solubility of iron carbonate and low kinetic parameters of the involved reactions make the corrosion process mainly undergo activation control. Mapped to the three stages shown in Figure 14, the low temperature extends greatly the developing time from Stage II to III.

Under alkaline environments, the highly depressed capacitive loop and a much lower characteristic frequency imply a huge difference in the corrosion process with acid. As discussed in Section 3.4.3, increasing pH may promote the accumulation of $(FeOH)_{ads}$, which makes the inductive loop undistinguished. However, there could be another explanation
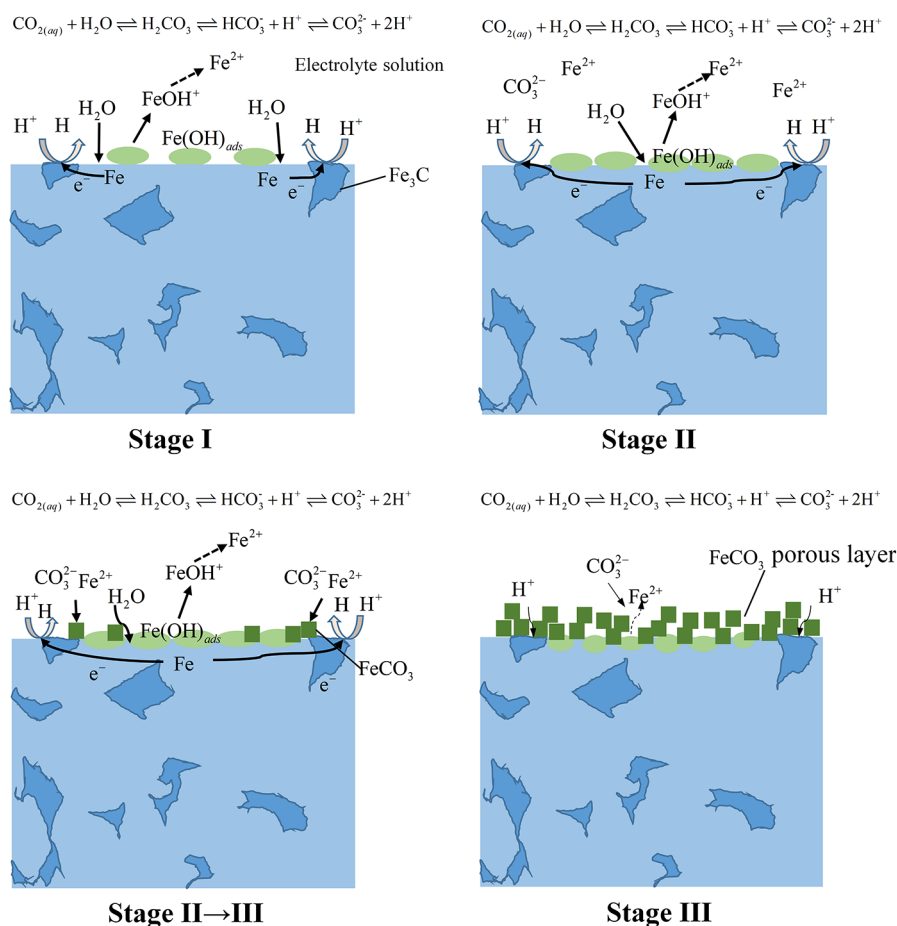

Figure 14. Diagrammatic sketch of the interfacial processes of three stages during exposure in carbon dioxide-saturated brines.

that the relaxation is hindered by increasing pH. Also, the latter seems to be more reasonable in concordance with the large polarization resistance. Under alkaline conditions, the developing time from Stage I to II is shortened critically.

4. CONCLUSIONS

The corrosion behavior of X80 pipeline steel in carbon dioxide-saturated solution was investigated by means of the LPR and EIS measurements. The following conclusions can be drawn.

At a temperature of 60 °C, three stages were presented during the whole exposure of 144 h; within the first stage (hours after exposure), both the polarization resistance R_p and the OCP are slightly changed, and the EIS result is characterized as a capacitive loop at the high frequency, an inductive loop, and a capacitive loop at a low frequency; at the second stage (during 24 h after exposure), both R_p and OCP increase greatly, and the inductive loop disappears along with the capacitive loop at a low frequency; at the third stage (tens of hours after exposure), R_p increases linearly with time, the growth of the OCP slows down, and another capacitive loop at a low frequency turns up.

The anodic reaction is first retarded by the accumulation of $(FeOH)_{ads}$ on the iron surface, which arouses a sharp increase in the OCP. As corrosion proceeds, a porous product layer gradually covers the surface of the working electrode, which reduces similarly the anodic and cathodic reactions.

An increase in salinity from 0.1 mol L^{-1} sodium chloride solution to 0.6 mol L^{-1} can promote the formation and relaxation of $(FeOH)_{ads}$, which reduces the polarization resistance and enhances iron dissolution as a result. However, the increase in salinity does not change the developing time of the three stages obviously.

At a low temperature of 20 °C, carbon dioxide corrosion is mainly under activation control, and a protective product layer is hard to form, which significantly prolongs the developing time from Stage II to III.

Increasing pH enlarges the polarization resistance and alters the interfacial process dramatically by impeding the relaxation of $(FeOH)_{ads}$.

It is convinced indirectly by these observations above that water adsorption is the dominant action on the iron surface at the initial stage during carbon dioxide corrosion of the steel.

In future work, the role that carbon dioxide plays in the evolution of corrosion products and the formation of a protective film on the steel surface under the influence of local water chemistry should be further studied.

■ AUTHOR INFORMATION

Corresponding Author

Yueshe Wang − State Key Laboratory of Multiphase Flow in Power Engineering, Xi'an Jiaotong University, Xi'an, Shaanxi 710049, China; Email: wangys@mail.xjtu.edu.cn

Authors

Jukai Chen − School of Chemical Engineering & Technology, China University of Mining and Technology, Xuzhou, Jiangsu 221116, China; ⊙ orcid.org/0000-0003-4603-1200

Xiaodan Wang − State Key Laboratory of Multiphase Flow in Power Engineering, Xi'an Jiaotong University, Xi'an, Shaanxi 710049, China

Honglian Ma − China Special Equipment Inspection and Research Institute, Beijing 100013, China

Zhiyuan Huo − State Key Laboratory of Multiphase Flow in Power Engineering, Xi'an Jiaotong University, Xi'an, Shaanxi 710049, China

Complete contact information is available at:
https://pubs.acs.org/10.1021/acsomega.1c06613

Notes

The authors declare no competing financial interest.

■ ACKNOWLEDGMENTS

■ REFERENCES

(1) Kermani, M. B.; Harrop, D. The Impact of Corrosion on the Oil and Gas Industry. *SPE Prod. Facil.* 1996, 11, 186−190.

(2) Kahyarian, A.; Singer, M.; Nesic, S. Modeling of Uniform CO_2 Corrosion of Mild Steel in Gas Transportation Systems: A Review. *J. Nat. Gas. Sci. Eng.* 2016, 29, 530−549.

(3) Moreira, R.; Bandeira, M.; Rocha, A.; Mattos, O. R. The Role of CO_2 on Carbon Steel Corrosion at Different CO_2 Pressure Levels. In *EUROCORR 2013*: Estoril, Portugal, September 1−5, 2013, Paper No. 1675.

(4) Almeida, T. C.; Bandeira, M. C. E.; Moreira, R. M.; Mattos, O. R. The Role of CO_2 on Carbon Steel Corrosion. In *CORROSION 2015*: Dallas, Texas, USA, March 15−19, 2015, Paper No. 5807.

(5) Almeida, T. C.; Bandeira, M. C. E.; Moreira, R. M.; Mattos, O. R. New Insights on the Role of CO_2 in the Mechanism of Carbon Steel Corrosion. *Corros. Sci.* 2017, 120, 239−250.

(6) Kahyarian, A.; Brown, B.; Nesic, S. Electrochemistry of CO_2 Corrosion of Mild Steel: Effect of CO_2 on Iron Dissolution Reaction. *Corros. Sci.* 2017, 129, 146−151.

(7) Kahyarian, A.; Nesic, S. A New Narrative for CO_2 Corrosion of Mild Steel. *J. Electrochem. Soc.* 2019, 166, C3048−C3063.

(8) Remita, E.; Tribollet, B.; Sutter, E.; Vivier, V.; Ropital, F.; Kittel, J. Hydrogen Evolution in Aqueous Solutions Containing Dissolved CO_2: Quantitative Contribution of the Buffering Effect. *Corros. Sci.* 2008, 50, 1433−1440.

(9) Bockris, J. O. M.; Drazic, D.; Despic, A. R. The Electrode Kinetics of the Deposition and Dissolution of Iron. *Electrochim. Acta* 1961, 4, 325−361.

(10) Li, P.; Tan, T. C.; Lee, J. Y. Impedance Spectra of the Anodic Dissolution of Mild Steel in Sulfuric Acid. *Corros. Sci.* 1996, 38, 1935−1955.

(11) Barcia, O. E.; Mattos, O. R. The Role of Chloride and Sulphate Anions in the Iron Dissolution Mechanism Studied by Impedance Measurements. *Electrochim. Acta* 1990, 35, 1003−1009.

(12) Keddam, M.; Mottos, O. R.; Takenouti, H. Reaction Model for Iron Dissolution Studied by Electrode Impedance: I. Experimental Results and Reaction Model. *J. Electrochem. Soc.* 1981, 128, 257−266.

(13) Keddam, M.; Mattos, O. R.; Takenouti, H. Reaction Model for Iron Dissolution Studied by Electrode Impedance II. Determination of the Reaction Model. *J. Electrochem. Soc.* 1981, 128, 266−274.

(14) Bechet, B.; Epelboin, I.; Keddam, M. New Data from Impedance Measurements Concerning the Anodic Dissolution of Iron in Acidic Sulphuric Media. *J. Electroanal. Chem. Interfacial Electrochem.* 1977, 76, 129−134.

(15) Almeida, T. C.; Bandeira, M. C. E.; Mattos, O. R.; Moreira, R. M. The Effect of High Partial Pressure of CO_2 on the Corrosion Mechanism of Carbon Steel in H_2O-CO_2 Systems. In *CORROSION 2018*: Phoenix, AZ, USA, April 15−19, 2018, Paper No. 11623.

(16) Li, S.; Zeng, Z.; Harris, M. A.; Sánchez, L. J.; Cong, H. CO_2 Corrosion of Low Carbon Steel Under the Joint Effects of Time-Temperature-Salt Concentration. *Front. Mater.* 2019, 6 (), DOI: 10.3389/fmats.2019.00010.

(17) Farelas, F.; Galicia, M.; Brown, B.; Nesic, S.; Castaneda, H. Evolution of Dissolution Processes at the Interface of Carbon Steel

Corroding in a CO_2 Environment Studied by EIS. *Corros. Sci.* **2010**, *52*, 509−517.

(18) Liu, Q. Y.; Mao, L. J.; Zhou, S. W. Effects of Chloride Content on CO_2 Corrosion of Carbon Steel in Simulated Oil and Gas Well Environments. *Corros. Sci.* **2014**, *84*, 165−171.

(19) Barker, R.; Burkle, D.; Charpentier, T.; Thompson, H.; Neville, A. A Review of Iron Carbonate ($FeCO_3$) Formation in the Oil and Gas Industry. *Corros. Sci.* **2018**, *142*, 312−341.

(20) Dugstad, A. Fundamental Aspects of CO_2 Metal Loss Corrosion-Part 1: Mechanism. In *CORROSION 2006*: Dallas, Texas, USA, March 15−19, 2015, Paper No. 06111.

(21) Kakooei, S.; Ismail, M. C.; Raja, B.; Mohebbi, H.; Emamian, S. S.; Moayedfar, M. Formation of Nano-Scale $FeCO_3$ Protective Corrosion Product in Carbon Dioxide-Saturated 3% Sodium Chloride Solution. *Key Eng. Mater.* **2017**, *740*, 3−8.

(22) Heuer, J. K.; Stubbins, J. F. An XPS Characterization of $FeCO_3$ Films from CO_2 Corrosion. *Corros. Sci.* **1999**, *41*, 1231−1243.

(23) Elgaddafi, R.; Ahmed, R.; Shah, S. Corrosion of Carbon Steel in CO_2 Saturated Brine at Elevated Temperatures. *J. Petrol. Sci. Eng.* **2021**, *196*, No. 107638.

(24) Burkle, D.; De Motte, R.; Taleb, W.; Kleppe, A.; Comyn, T.; Vargas, S. M.; Neville, A.; Barker, R. In Situ SR-XRD Study of $FeCO_3$ Precipitation Kinetics onto Carbon Steel in CO_2-Containing Environments: The Influence of Brine pH. *Electrochim. Acta* **2017**, *255*, 127−144.

(25) Berntsen, T.; Seiersten, M.; Hemmingsen, T. Effect of $FeCO_3$ Supersaturation and Carbide Exposure on the CO_2 Corrosion Rate of Carbon Steel. *Corrosion* **2013**, *69*, 601−613.

(26) Farelas, F.; Brown, B.; Nesic, S. Iron Carbide and its Influence on the Formation of Protective Iron Carbonate in CO2 Corrosion of Mild Steel. In *CORROSION 2013*: Orlando, Florida, USA, March 17−21, 2013, Paper No. 2291.

(27) Almeida, T. C.; Bandeira, M. C. E.; Moreira, R. M.; Mattos, O. R. Discussion on "Electrochemistry of CO_2 corrosion of mild steel: Effect of CO_2 on iron dissolution reaction" by A. Kahyarian, B. Brown, S. Nesic, [Corros. Sci. 129 (2017) 146−151]. *Corros. Sci.* , **2018** (), 417−422, DOI: 10.1016/j.corsci.2018.02.004.

(28) Almeida, T. C.; Barcia, O. E.; Moreira, R. M.; Bandeira, M. C. E.; Mattos, O. R. Discussion and Challenges Concerning the Elaboration of a Dissolution Reaction Mechanism. *Electrochim. Acta* **2019**, *303*, 211−218.

(29) Joshi, G. R. Elucidating Sweet Corrosion Scales. Ph.D. Thesis, the University of Manchester, Manchester, UK, 2015.

(30) Lee, K.-L. J. A Mechanistic Modeling of CO_2 Corrosion of Mild Steel in the Presence of H_2S. Ph.D. Thesis, Ohio University, Athens, OH, USA, 2004.

(31) Zhang, G. A.; Liu, D.; Li, Y. Z.; Guo, X. P. Corrosion Behaviour of N80 Carbon Steel in Formation Water under Dynamic Supercritical CO_2 Condition. *Corros. Sci.* **2017**, *120*, 107−120.

(32) Zhu, S. D.; Fu, A. Q.; Miao, J.; Yin, Z. F.; Zhou, G. S.; Wei, J. F. Corrosion of N80 Carbon Steel in Oil Field Formation Water Containing CO_2 in the Absence and Presence of Acetic Acid. *Corros. Sci.* **2011**, *53*, 3156−3165.

(33) Sun, W.; Nešić, S.; Woollam, R. C. The Effect of Temperature and Ionic Strength on Iron Carbonate ($FeCO_3$) Solubility Limit. *Corros. Sci.* **2009**, *51*, 1273−1276.

(34) Chen, J.; Wang, X.; Wang, Y.; Huang, H. Numerical Simulation of Carbon Dioxide Corrosion under Flow Conditions in an Elbow. *Materwiss. Werksttech.* **2019**, *50*, 442−453.